Unified Impedance Model of Grid-Connected Voltage-Source Converters

Wang, Xiongfei; Harnefors, Lennart; Blaabjerg, Frede

Published in:
I E E E Transactions on Power Electronics

DOI (link to publication from Publisher):
10.1109/TPEL.2017.2684906

Publication date:
2018

Document Version
Publisher's PDF, also known as Version of record

Citation for published version (APA):
Wang, X., Harnefors, L., & Blaabjerg, F. (2018). Unified Impedance Model of Grid-Connected Voltage-Source Converters. *I E E E Transactions on Power Electronics*, *33*(2), 1775 - 1787. Article 7913725. https://doi.org/10.1109/TPEL.2017.2684906

Unified Impedance Model of Grid-Connected Voltage-Source Converters

Xiongfei Wang, *Member, IEEE*, Lennart Harnefors, *Fellow, IEEE*, and Frede Blaabjerg, *Fellow, IEEE*

***Abstract*—This paper proposes a unified impedance model of grid-connected voltage-source converters for analyzing dynamic influences of the phase-locked loop (PLL) and current control. The mathematical relations between the impedance models in the different domains are first explicitly revealed by means of complex transfer functions and complex space vectors. A stationary ($\alpha\beta$-) frame impedance model is then proposed, which not only predicts the stability impact of the PLL, but also reveals its frequency coupling effect. Furthermore, the impedance shaping effects of the PLL on the current control in the rotating (*dq*-) frame and the stationary ($\alpha\beta$-) frame are structurally comapred. The frequency-domain case studies on a three-phase grid-connected converter are next presented, and subsequently validated in time-domain simulations and experimental tests. The close correlations between the measured results and theoretical analysis confirm the effectiveness of the stationary-frame impedance model.**

***Index Terms*—Grid, impedance model, phase-locked loop (PLL), stability, voltage-source converters (VSCs).**

I. INTRODUCTION

VOLTAGE-SOURCE converters (VSCs) are increasingly used in electric power grids for efficient energy consumption and renewable energy generation [1]. Compared to electrical machines, VSCs have the wider bandwidth control dynamics, ranging from the outer power control loops (subsynchronous frequencies) to the inner current control loop (hundreds of hertz to kHz). The dynamic interactions among the power grid and VSCs tend to cause oscillations in a wide frequency range [2].

To address the stability challenges with the grid-connected VSCs, the impedance modeling and control methods have been developed for dynamic characterization and active stabilization of VSCs [3]–[10]. However, many of the research efforts were dedicated to the stability of the inner current control with *LCL*-filters [3]–[6], where the influences of current controller and time delay of the digital control system have been thoroughly discussed. Only a few works have recently been reported to include the effects of the grid synchronization and the outer power (dc-link voltage) control loops [7]–[10], [16], [17]. Those control loops are usually designed with a lower bandwidth than the current control, which, together with the grid impedance, tend to result in the unexpected harmonics or resonances near the fundamental frequency [2].

A wide variety of grid synchronization schemes have been reported for grid-connected VSCs. The synchronous reference frame phase-locked loop (SRF-PLL), among other schemes, has widely been used with single-phase and three-phase VSCs [11]–[14]. In the SRF-PLL, the phase detection is realized by using the Park (*dq*-) transformation, which is highly nonlinear and time-variant, and hence significantly complicates the small-signal modeling of the SRF-PLL [7]. Moreover, only the *q*-axis component is regulated for the phase tracking, which, unlike the current control, leads to an asymmetric *dq*-frame model [15], and consequently brings in a frequency coupling effect in the phase domain [2], [16], [17].

Two impedance models have, thus, been developed to reveal the dynamic influence of the PLL. In the first approach, the impedance model was developed in the rotating *dq*-frame [7]–[9], where two *dq*-frames, which are aligned to the measured and actual grid phase, respectively, were built. Thus, the PLL dynamics can be accounted by linearizing the transformation between the two frames [7]. The *dq*-frame model effectively predicts the stability impact of the SRF-PLL by means of the generalized Nyquist stability criterion. However, it fails to reveal how the impedance characteristics of the grid and VSCs contribute to the frequencies of the induced oscillations, since both the VSC output impedance and grid impedance are nondiagonal transfer matrices in the *dq*-frame [18].

The second method is based on the principle of harmonic balance, where the harmonic linearization of sinusoidal signals is employed to formulate the impedance model directly in the stationary $\alpha\beta$-frame [10]. Such a representation simplifies the model as a diagonal transfer matrix, which is composed by two single-input single-output transfer functions for modeling the VSC system in the positive-sequence and negative-sequence, and it is hence also named as the sequence-domain impedance model [17]. Compared to the *dq*-frame model, the $\alpha\beta$-frame model facilitates the stability analysis of multiple-VSC-based systems, where the whole system can be readily modeled in a common frame, rather than using multiple *dq*-frames for multiple VSCs [19]. However, the $\alpha\beta$-frame model in [10] neglects the frequency-coupling effect brought by the

---

Manuscript received August 3, 2016; revised December 1, 2016; accepted February 14, 2017. Date of publication April 27, 2017; date of current version November 2, 2017. This work was supported by the European Research Council under the European Union's Seventh Framework Program (FP7/2007-2013)/ERC Grant Agreement no. 321149-Harmony. Recommended for publication by Associate Editor Marta Molinas. *(Corresponding author: Xiongfei Wang.)*

X. Wang and F. Blaabjerg are with the Department of Energy Technology, Aalborg University, Aalborg 9220, Denmark (e-mail: xwa@et.aau.dk; fbl@et.aau.dk).

L. Harnefors is with the ABB Corporate Research, Västerås 72178, Sweden (e-mail: lennart.harnefors@se.abb.com).

Color versions of one or more of the figures in this paper are available online at http://ieeexplore.ieee.org.

Digital Object Identifier 10.1109/TPEL.2017.2684906

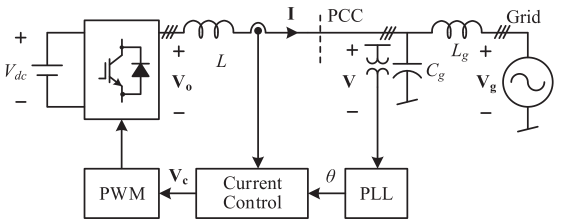

Fig. 1. Simplified one-line diagram of a three-phase grid-connected VSC.

TABLE I
MAIN CIRCUIT PARAMETERS

Symbol	Electrical Constant	Value (p.u.)
V_g	Grid voltage (line-to-line)	400 V (1)
f_1	Grid fundamental frequency	50 Hz (1)
L_g	Grid inductance	5 mH (0.139)
C_g	Grid capacitance	20 μF (0.071)
f_{sw}	VSC switching frequency	10 kHz (200)
f_s	VSC control sampling frequency	10 kHz (200)
V_{dc}	Inverter dc-link voltage	730 V (1.825)
L	VSC filter inductor	3 mH (0.083)
I_{d0}	Steady-state output current (*d*-axis)	15 A (1.414)
I_{q0}	Steady-state output current (*q*-axis)	0 A (0)

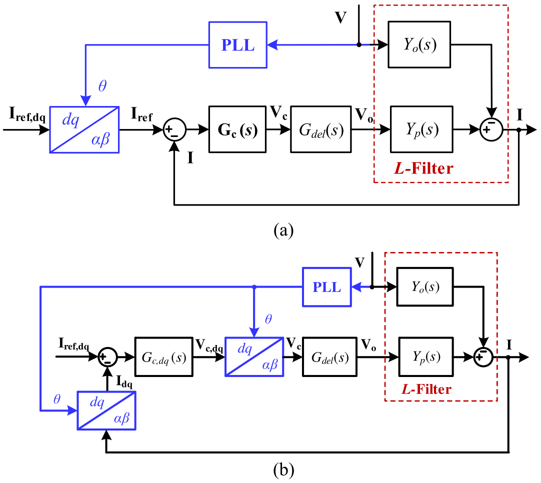

Fig. 2. Block diagrams of the current control loop in the different frames. (a) $\alpha\beta$-frame current control. (b) *dq*-frame current control.

dq-transformation, which may lead to the inaccurate stability prediction [16].

Considering the frequency-coupling dynamics, a modified sequence-domain impedance model has been discussed in [16] and [17]. It is found that the same stability implication as the *dq*-frame impedance model can be observed, provided that the frequency-coupling transfer functions are included. Yet, the mathematical relations between the modified sequence-domain model given in [16] and the *dq*-frame model are not revealed. A transformation matrix has, thus, been introduced in [17] in order to establish the mathematical relations between the impedance models in the *dq*-frame and the sequence-domain. However, the frequency translation between the transfer functions in the *dq*-frame and $\alpha\beta$-frame [15] is overlooked in the transformation matrix reported in [17]. Hence, it merely transforms the original *dq*-frame transfer matrix, which is based on real space vectors, into another *dq*-frame transfer matrix based on complex space vectors. Furthermore, for space vectors in the $\alpha\beta$-frame, their positive and negative frequencies ($\pm\omega$) represent the positive-sequence and negative-sequence components at the frequency ω [15]. Thus, the modified sequence-domain model in [17] may yield a void sequence component without physical meaning, e.g., a negative-sequence component with a negative frequency.

To explicitly reveal the mathematical relations between the models developed in the different domains, this paper proposes a unifying approach by means of complex space vectors and complex transfer functions [15]. An impedance model in the $\alpha\beta$-frame is derived from the unifying approach, which not only identifies the transfer functions capturing frequency-coupling dynamics of space vectors, but also removes the void sequence component in the modified sequence-domain impedance model [17]. Moreover, the impedance shaping effect of the PLL for the *dq*-frame and the $\alpha\beta$-frame current control is structurally compared. Stability analysis based on the proposed impedance model is performed. It is found that the $\alpha\beta$-frame current control with the fixed-line-frequency resonant controller is more robust than the *dq*-frame current control against the PLL effect. Time-domain simulations and experiments validate the effectiveness of the impedance model and the frequency-domain analysis.

II. GRID-CONNECTED VSCS

A. System Description

Fig. 1 illustrates a simplified one-line diagram of a three-phase grid-connected VSC, where a constant dc-link voltage (V_{dc}) is assumed, and a paralleled *LC*-type grid impedance is considered. Table I provides the main circuit parameters. The voltage at the point of common coupling (PCC) is measured for synchronizing the VSC with the grid by means of the PLL. The current control can be realized with either the proportional + resonant (PR) controller in the $\alpha\beta$-frame or the P + integral (PI) controller in the *dq*-frame.

For clarity, bold letters are used in this paper to denote complex space vectors, e.g., $\mathbf{V} = V_\alpha + jV_\beta$ and $\mathbf{I} = I_\alpha + jI_\beta$ for the PCC voltage and VSC current, respectively, and complex transfer functions, e.g., the admittance $\mathbf{Y}(s) = Y_\alpha(s) + jY_\beta(s)$ [15]. The corresponding real space vectors are represented by italic letters, e.g., $V = [V_\alpha, V_\beta]^T \leftrightarrow \mathbf{V}$ and $I = [I_\alpha, I_\beta]^T \leftrightarrow \mathbf{I}$. A subscript "*dq*" is added for space vectors and transfer functions referred to the *dq*-frame, e.g., $\mathbf{V_{dq}} = V_d + jV_q$ and $\mathbf{Y_{dq}}(s) = Y_d(s) + jY_q(s)$ for the PCC voltage and admittance in the rotating *dq*-frame, respectively. Transfer matrices are denoted with an additional superscript "*m*," and the matrices of complex transfer functions are represented by bold letters.

B. Current Control Model

Fig. 2 depicts the block diagrams for the current control implemented in the $\alpha\beta$-frame, as shown in Fig. 2(a), and in the *dq*-frame, see Fig. 2(b). In the $\alpha\beta$-frame, the *L*-filter plant can be represented by the following transfer functions:

$$Y_p(s)=\left.\frac{\mathbf{I}}{\mathbf{V_o}}\right|_{\mathbf{V}=0}=\frac{1}{Ls+R_L},\quad Y_o(s)=\left.\frac{\mathbf{I}}{\mathbf{V}}\right|_{\mathbf{V_o}=0}=\frac{1}{Ls+R_L} \tag{1}$$

where the VSC output voltage is denoted by the complex space vector $\mathbf{V_o}=V_{o\alpha}+jV_{o\beta}$, in the $\alpha\beta$-frame. R_L is the equivalent series resistance of the filter inductor. Then, based on the frequency translation between the $\alpha\beta$-frame and *dq*-frame [15], the *L*-filter plant in the *dq*-frame can be derived as following:

$$\begin{aligned}&\mathbf{I}=Y_p(s)\mathbf{V_o}\\ &\quad\Rightarrow \mathbf{I_{dq}}=e^{-j\theta}Y_p(s)e^{j\theta}\mathbf{V_{o,dq}}=Y_p(s+j\omega_1)\mathbf{V_{o,dq}}\\ &\quad\Rightarrow \mathbf{Y_{p,dq}}(s)=Y_p(s+j\omega_1)\\ &\mathbf{Y_{o,dq}}(s)=Y_o(s+j\omega_1)=Y_p(s+j\omega_1)=\frac{1}{L(s+j\omega_1)+R_L}\end{aligned} \tag{2}$$

where $e^{-j\theta}=\cos(\theta)-j\sin(\theta)$ is the complex form of the Park transformation [7], and $e^{j\theta}$ is the inverse Park transformation. ω_1 is the grid fundamental frequency (i.e., line frequency).

$G_{c,dq}(s)$ is the PI current controller in the *dq*-frame, which is given by

$$G_{c,dq}(s)=k_p+\frac{k_i}{s}. \tag{3}$$

Following the frequency translation, $G_{c,dq}(s)$ is transformed in the $\alpha\beta$-frame as

$$\mathbf{G_c}(s)=G_{c,dq}(s-j\omega_1)=k_p+\frac{k_i}{s-j\omega_1} \tag{4}$$

where the center frequency ω_1 is fixed in the $\alpha\beta$-frame current control, yet it is equivalently adapted to the PLL dynamics in the *dq*-frame current control.

$G_{\mathrm{del}}(s)$ is the time delay of the digital control system, which, in the worst case, includes one sampling period (T_s) of the computational delay and half-sampling period $(0.5T_s)$ delay of the pulse width modulator [20]:

$$G_{\mathrm{del}}(s)=e^{-1.5T_s s}. \tag{5}$$

The closed-loop response of the $\alpha\beta$-frame current control can, thus, be derived as follows:

$$\mathbf{I}=\mathbf{G_{cl}}(s)\mathbf{I_{ref}}-Y_{cl}(s)\mathbf{V} \tag{6}$$

$$\mathbf{G_{cl}}(s)=\frac{\mathbf{T}(s)}{1+\mathbf{T}(s)},\quad \mathbf{Y_{cl}}(s)=\frac{Y_o(s)}{1+\mathbf{T}(s)} \tag{7}$$

where $\mathbf{G_{cl}}(s)$ and $\mathbf{Y_{cl}}(s)$ are the closed-loop gain and control output admittance of the $\alpha\beta$-frame current control, respectively. $\mathbf{T}(s)$ denotes the open-loop gain of the $\alpha\beta$-frame current control, which is given by

$$\mathbf{T}(s)=\mathbf{G_c}(s)G_{\mathrm{del}}(s)Y_p(s). \tag{8}$$

Similarly, the open-loop gain of the *dq*-frame current control can be derived as

$$\mathbf{T_{dq}}(s)=G_{c,dq}(s)G_{\mathrm{del}}(s)\mathbf{Y_{p,dq}}(s). \tag{9}$$

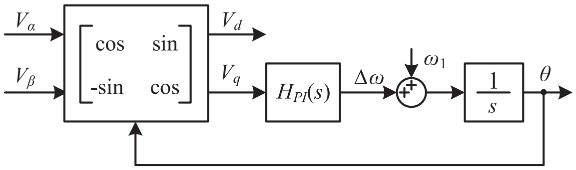

Fig. 3. Block diagram of the SRF-PLL.

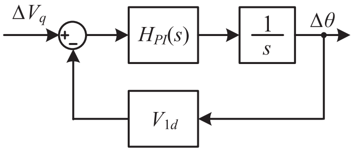

Fig. 4. Block diagram of the small-signal model of the SRF-PLL.

The closed-loop response of the current loop in the *dq*-frame is expressed as

$$\mathbf{I_{dq}}=\mathbf{G_{cl,dq}}(s)\mathbf{I_{ref,dq}}-\mathbf{Y_{cl,dq}}(s)\mathbf{V_{dq}} \tag{10}$$

$$\mathbf{G_{cl,dq}}(s)=\frac{\mathbf{T_{dq}}(s)}{1+\mathbf{T_{dq}}(s)},\quad \mathbf{Y_{cl,dq}}(s)=\frac{\mathbf{Y_{o,dq}}(s)}{1+\mathbf{T_{dq}}(s)}. \tag{11}$$

C. PLL Model

Fig. 3 depicts the block diagram of the SRF-PLL adopted in this work, where the *dq*-transformation is used for the phase detection, and the *q*-axis voltage is regulated by a PI controller for the phase tracking [11].

Given a perturbation on the PCC voltage in the *dq*-frame $\Delta\mathbf{V_{dq}}$, the PCC voltage in the $\alpha\beta$-frame can be expressed as

$$\mathbf{V}=(V_{1d}+\Delta\mathbf{V_{dq}})e^{j\omega_1 t} \tag{12}$$

where V_{1d} is the steady-state PCC voltage aligned to the *d*-axis, i.e., the steady-state PCC voltage vector $\mathbf{V_{1,dq}}=V_{1d}+j0$. The response of the detected phase θ corresponding to the voltage perturbation can be given as

$$\theta=\omega_1 t+\Delta\theta. \tag{13}$$

The *q*-axis voltage at the output of the *dq*-transformation is, thus, derived as follows:

$$\begin{aligned}\mathbf{V_{dq}}&=\mathbf{V}e^{-j\theta}=(V_{1d}+\Delta\mathbf{V_{dq}})e^{-j\Delta\theta}\\ &\approx(V_{1d}+\Delta\mathbf{V_{dq}})(1-j\Delta\theta)\Rightarrow V_q=\Delta V_q-\Delta\theta V_{1d}.\end{aligned} \tag{14}$$

Then, considering the PI controller, the detected phase variation $\Delta\,\theta$ is given by

$$\Delta\theta=\frac{H_{\mathrm{PI}}(s)}{s}V_q. \tag{15}$$

Substituting (15) into (14), the small-signal model of the SRF-PLL can, thus, be established, which, as shown in Fig. 4, can be derived as [2]

$$\Delta\theta=H_{\mathrm{PLL}}(s)\Delta V_q,\quad H_{\mathrm{PLL}}(s)=\frac{H_{\mathrm{PI}}(s)}{s+H_{\mathrm{PI}}(s)V_{1d}} \tag{16}$$

which illustrates that SRF-PLL is linearized as a second-order dynamic system.

III. UNIFIED IMPEDANCE MODEL WITH PLL EFFECT

This section elaborates first the *dq*-frame impedance model built upon the *dq*-frame current control with the PLL dynamics [2], [7]–[9]. Then, a unifying approach to the impedance models in the different domains is proposed by using complex space vectors and complex transfer functions. It further reveals that the transformation matrix introduced in [17] merely transforms a *dq*-frame impedance matrix of real space vectors into another *dq*-frame impedance matrix based on complex space vectors.

A. DQ-Frame Impedance Model

Similar to (14), the *dq*-transformations used within the *dq*-frame current control can also be linearized as follows:

$$\begin{aligned}\mathbf{I_{dq}} &= \mathbf{I}e^{-j\theta} = (\mathbf{I_{1,dq}} + \Delta\mathbf{I_{dq}})e^{-j\Delta\theta}\\ &\approx (\mathbf{I_{1,dq}} + \Delta\mathbf{I_{dq}})(1 - j\Delta\theta)\\ &\Rightarrow \mathbf{I_{dq}} = \mathbf{I_{1,dq}} + \Delta\mathbf{I_{dq}} - \Delta\mathbf{I_{PLL,dq}}\\ &\quad\ \Delta\mathbf{I_{PLL,dq}} = j\Delta\theta\mathbf{I_{1,dq}}\end{aligned}\tag{17}$$

$$\begin{aligned}\mathbf{V_c} &= \mathbf{V_{c,dq}}e^{j\theta} = (\mathbf{V_{c1,dq}} + \Delta\mathbf{V_{c,dq}})e^{j(\omega_1 t + \Delta\theta)}\\ &\approx (\mathbf{V_{c1,dq}} + \Delta\mathbf{V_{c,dq}})(1 + j\Delta\theta)e^{j\omega_1 t}\\ &\Rightarrow \mathbf{V_{c,dq}} = \mathbf{V_{c1,dq}} + \Delta\mathbf{V_{c,dq}} + \Delta\mathbf{V_{PLL,dq}}\\ &\quad\ \Delta\mathbf{V_{PLL,dq}} = j\Delta\theta\mathbf{V_{c1,dq}}\end{aligned}\tag{18}$$

where $\mathbf{I_{1,dq}} = I_{1d} + jI_{1q}$ is the steady-state VSC current. $\mathbf{V_{c1,\,dq}} = V_{c1d} + jV_{c1q}$ is the steady-state modulating voltage. $\Delta\mathbf{I_{PLL,\,dq}}$ and $\Delta\mathbf{V_{PLL,\,dq}}$ denote the dynamic effects of the PLL on the VSC current and the voltage reference of the modulator, respectively.

Substituting (16) into (17) and (18) leads to

$$\begin{aligned}\Delta\mathbf{I_{PLL,dq}} &= jH_{\text{PLL}}(s)\mathbf{I_{1,dq}}\Delta V_q\\ \Delta\mathbf{V_{PLL,dq}} &= jH_{\text{PLL}}(s)\mathbf{V_{c1,dq}}\Delta V_q\end{aligned}\tag{19}$$

where the input is merely the *q*-axis voltage, other than space vectors in (10), which are derived for the current loop only. Hence, asymmetric transfer matrices with the cross-couplings between the *d*- and *q*-axis components are inevitable when the dynamics of PLL are included [7]–[9], [15].

Fig. 5 illustrates the block diagram of transfer matrices for the *dq*-frame current control with the PLL effect. The transfer functions in Fig. 2(b) are represented by the symmetric transfer matrices, which are denoted with the additional superscript "*m*," i.e., the transfer functions for the current controller $G_{c,dq}(s)$, the time delay $G_{\text{del}}(s)$, and the *L*-filter plant $Y_{p,dq}(s)$ are changed, respectively, as

$$G_{c,dq}(s) \to G_{c,dq}^m(s) = \begin{bmatrix} G_{c,dq}(s) & 0\\ 0 & G_{c,dq}(s)\end{bmatrix}$$

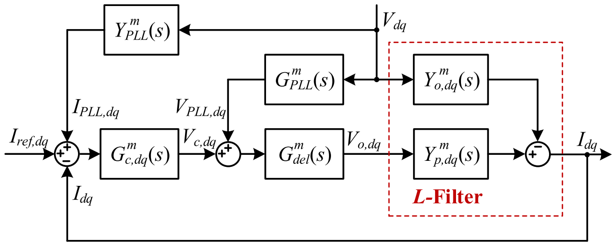

Fig. 5. Block diagram of transfer matrices for the *dq*-frame current control with the small-signal dynamics of the PLL.

$$G_{\text{del}}(s) \to G_{\text{del}}^m(s) = \begin{bmatrix} G_{\text{del}}(s) & 0\\ 0 & G_{\text{del}}(s)\end{bmatrix}\tag{20}$$

$$Y_{p,dq}(s) \to Y_{p,dq}^m(s) = \frac{1}{L(s^2 + \omega_1^2)}\begin{bmatrix} s & \omega_1\\ -\omega_1 & s\end{bmatrix} = Y_{o,dq}^m(s).\tag{21}$$

Based on (19), the PLL effects are modeled by two asymmetric transfer matrices, $Y_{\text{PLL}}^m(s)$ and $G_{\text{PLL}}^m(s)$, which are given by

$$\begin{aligned}I_{\text{PLL},dq} &= \begin{bmatrix} I_{\text{PLL},d}\\ I_{\text{PLL},q}\end{bmatrix} = \underbrace{\begin{bmatrix} 0 & -H_{\text{PLL}}(s)I_{1q}\\ 0 & H_{\text{PLL}}(s)I_{1d}\end{bmatrix}}_{Y_{\text{PLL}}^m(s)}\begin{bmatrix} V_d\\ V_q\end{bmatrix}\\ V_{\text{PLL},dq} &= \begin{bmatrix} V_{\text{PLL},d}\\ V_{\text{PLL},q}\end{bmatrix} = \underbrace{\begin{bmatrix} 0 & -H_{\text{PLL}}(s)V_{c1q}\\ 0 & H_{\text{PLL}}(s)V_{c1d}\end{bmatrix}}_{G_{\text{PLL}}^m(s)}\begin{bmatrix} V_d\\ V_q\end{bmatrix}\end{aligned}\tag{22}$$

where the symbol "Δ" is omitted for simplicity. By shifting the output of $G_{\text{PLL}}^m(s)$ to the output of $Y_{\text{p,dq}}^m(s)$ in Fig. 5, it can be seen that the open-loop output admittance is reshaped by the PLL effect on the modulating voltage $G_{\text{PLL}}^m(s)$, which is then changed as $Y_{to,dq}^m(s)$, and given by

$$Y_{\text{to},dq}^m(s) = Y_{o,dq}^m(s) - Y_{p,dq}^m(s)G_{\text{del}}^m(s)G_{\text{PLL}}^m(s).\tag{23}$$

However, the open-loop gain of the current control loop is kept the same as (9) [21].

Including then the PLL effect on the VSC current $Y_{\text{PLL}}^m(s)$, the modified closed-loop current response is derived as

$$\begin{aligned}I_{dq} &= \begin{bmatrix} I_d\\ I_q\end{bmatrix} = G_{\text{cl},dq}^m(s)\begin{bmatrix} I_{\text{ref},d}\\ I_{\text{ref},q}\end{bmatrix}\\ &\quad - \underbrace{\left\{[I^m + T_{dq}^m(s)]^{-1}Y_{\text{to},dq}^m(s) - G_{\text{cl},dq}^m(s)Y_{\text{PLL}}^m(s)\right\}}_{Y_{\text{tcl},dq}^m(s)}\begin{bmatrix} V_d\\ V_q\end{bmatrix}\end{aligned}\tag{24}$$

where I^m is the unitary diagonal matrix, $T_{cl,dq}^m(s)$ and $G_{cl,dq}^m(s)$, are symmetric transfer matrices for the open-loop and closed-loop gains of the current loop, respectively, which are

$$\begin{aligned}I^m &= \begin{bmatrix} 1 & 0\\ 0 & 1\end{bmatrix},\quad T_{dq}^m(s) = Y_{p,dq}^m(s)G_{\text{del}}^m(s)G_{c,dq}^m(s)\\ G_{\text{cl},dq}^m(s) &= [I^m + T_{dq}^m(s)]^{-1}T_{dq}^m(s).\end{aligned}\tag{25}$$

$Y^m_{\text{tcl,dq}}(s)$ is the modified closed-loop control output admittance matrix with the PLL dynamics.

B. Unifying Approach

Basically, a second-order transfer matrix based on real space vectors can be transformed as two complex transfer functions for the corresponding complex space vector and its conjugate [15]. This complex equivalence leads to a unifying approach to the *dq*-frame impedance model [7]–[9] and the modified sequence-domain impedance model [17].

For illustration, a generic *dq*-frame impedance matrix is used first to reveal the mathematical relations between the models in the different domains. Given a general *dq*-frame impedance matrix $Z^m_{\text{dq}}(s)$, which is expressed by

$$V_{dq} = \begin{bmatrix} V_d \\ V_q \end{bmatrix} = Z^m_{dq}(s)\begin{bmatrix} I_d \\ I_q \end{bmatrix}, \quad Z^m_{dq}(s) = \begin{bmatrix} Z_{dd}(s) & Z_{dq}(s) \\ Z_{qd}(s) & Z_{qq}(s) \end{bmatrix} \tag{26}$$

its complex equivalent can be derived in the following [2], [15]:

$$\mathbf{V_{dq}} = \mathbf{Z_{+,dq}}(s)\mathbf{I_{dq}} + \mathbf{Z_{-,dq}}(s)\mathbf{I^*_{dq}} \tag{27}$$

$$\mathbf{Z_{+,dq}}(s) = \frac{Z_{dd}(s) + Z_{qq}(s)}{2} + j\frac{Z_{qd}(s) - Z_{dq}(s)}{2}$$

$$\mathbf{Z_{-,dq}}(s) = \frac{Z_{dd}(s) - Z_{qq}(s)}{2} + j\frac{Z_{qd}(s) + Z_{dq}(s)}{2} \tag{28}$$

where $\mathbf{I^*_{dq}}$ is the complex conjugate of $\mathbf{I_{dq}}$. $\mathbf{Z_{+,dq}}(s)$ and $\mathbf{Z_{-,dq}}(s)$ are the equivalent complex transfer functions. If the impedance matrix is symmetric, i.e., $Z_d\,(\mathrm{s}) = Z_{dd}(s) = Z_{qq}(s)$ and $Z_q\,(s) = Z_{qd}(s) = -Z_{dq}(s)$ [15], its complex equivalent will be simplified as a single complex transfer function $\mathbf{Z_{dq}}(s)$, which is given by

$$\mathbf{V_{dq}} = \mathbf{Z_{dq}}(s)\mathbf{I_{dq}}, \quad \mathbf{Z_{dq}}(s) = Z_d(s) + jZ_q(s). \tag{29}$$

However, if the impedance matrix is asymmetric, the conjugate of the complex space vector will be required, as expressed in (27). The asymmetric impedance matrix based on real space vectors consequently results in a double-frequency model with complex space vectors.

To capture the frequency-coupled dynamics of the double-frequency model, a complex transfer function matrix $\mathbf{Z^m_{\pm,dq}}(s)$ is proposed in this work, which is given by

$$\begin{bmatrix} \mathbf{V_{dq}} \\ \mathbf{V^*_{dq}} \end{bmatrix} = \underbrace{\begin{bmatrix} \mathbf{Z_{+,dq}}(s) & \mathbf{Z_{-,dq}}(s) \\ \mathbf{Z^*_{-,dq}}(s) & \mathbf{Z^*_{+,dq}}(s) \end{bmatrix}}_{\mathbf{Z^m_{\pm,dq}}(s)} \begin{bmatrix} \mathbf{I_{dq}} \\ \mathbf{I^*_{dq}} \end{bmatrix} \tag{30}$$

where $\mathbf{Z^*_{+,dq}}\ (s)$ and $\mathbf{Z^*_{-,dq}}\ (s)$ are the complex conjugates of the complex transfer functions $\mathbf{Z_{+,dq}}(s)$ and $\mathbf{Z_{-,dq}}(s)$, respectively. The complex transfer matrix is the essential idea of the unifying approach.

In the modified sequence-domain impedance model [17], a linear transformation matrix A_z is introduced to transform the impedance matrix *Zm dq*(*s*) into the sequence-domain. However, it is worth noting that the resulting impedance matrix in [17] is also a complex transfer matrix based on complex space vectors, and it is actually equal to the impedance matrix $\mathbf{Z}^{\boldsymbol{m}}_{\pm,\mathbf{dq}}(s)$ derived in (30), i.e.,

$$\mathbf{Z^m_{pn}}(s) = A_Z Z^m_{dq}(s) A_Z^{-1} = \mathbf{Z^m_{\pm,dq}}(s). \tag{31}$$

Hence, the transformed impedance matrix in [17] is still in the *dq*-frame, other than in the sequence-domain or in the $\alpha\beta$-frame. Moreover, the complex equivalence given in (27) reveals the mathematical relations between the *dq*-frame model and the modified sequence-domain model in [17]. Yet, the frequency translation from the *dq*-frame to $\alpha\beta$-frame is still overlooked in (31), and thus the frequency coupling effect revealed in [2] and [16] is not explicitly identified.

IV. STATIONARY-FRAME IMPEDANCE MODEL

This section introduces first the proposed impedance model in the $\alpha\beta$-frame, and then presents a structural comparison of the impedance shaping effects of the PLL on the *dq*-frame and $\alpha\beta$-frame current control.

A. Proposed $\alpha\beta$-Frame Impedance Model

Considering the frequency translation of complex transfer functions [15], the complex transfer matrix in (30) and (31) can be further transformed into the $\alpha\beta$-frame, which is elaborated in the following:

$$\begin{aligned} e^{-j\theta}\mathbf{V} &= \mathbf{Z_{+,dq}}(s)e^{-j\theta}\mathbf{I} + \mathbf{Z_{-,dq}}(s)e^{j\theta}\mathbf{I}^* \\ &\Rightarrow \mathbf{V} = e^{j\theta}\mathbf{Z_{+,dq}}(s)e^{-j\theta}\mathbf{I} + e^{j\theta}\mathbf{Z_{-,dq}}(s)e^{j\theta}\mathbf{I}^* \\ &= \mathbf{Z_{+,dq}}(s - j\omega_1)\mathbf{I} + \mathbf{Z_{-,dq}}(s - j\omega_1)e^{j2\theta}\mathbf{I}^* \end{aligned} \tag{32}$$

$$\begin{aligned} e^{j\theta}\mathbf{V}^* &= \mathbf{Z^*_{-,dq}}(s)e^{-j\theta}\mathbf{I} + \mathbf{Z^*_{+,dq}}(s)e^{j\theta}\mathbf{I}^* \\ &\Rightarrow e^{j2\theta}\mathbf{V}^* = e^{j\theta}\mathbf{Z^*_{-,dq}}(s)e^{-j\theta}\mathbf{I} + e^{j\theta}\mathbf{Z^*_{+,dq}}(s)e^{j\theta}\mathbf{I}^* \\ &= \mathbf{Z^*_{-,dq}}(s - j\omega_1)\mathbf{I} + \mathbf{Z^*_{+,dq}}(s - j\omega_1)e^{j2\theta}\mathbf{I}^* \end{aligned} \tag{33}$$

$$\begin{bmatrix} \mathbf{V} \\ e^{j2\theta}\mathbf{V}^* \end{bmatrix} = \underbrace{\begin{bmatrix} \mathbf{Z_{+,dq}}(s - j\omega_1) & \mathbf{Z_{-,dq}}(s - j\omega_1) \\ \mathbf{Z^*_{-,dq}}(s - j\omega_1) & \mathbf{Z^*_{+,dq}}(s - j\omega_1) \end{bmatrix}}_{\mathbf{Z^m_{\pm}}(s)} \begin{bmatrix} \mathbf{I} \\ e^{j2\theta}\mathbf{I}^* \end{bmatrix} \tag{34}$$

where $\mathbf{I}^*$ is the complex conjugate of $\mathbf{I}$ in the $\alpha\beta$-frame, $\mathbf{Z^m_{\pm}}(s)$ is the complex transfer matrix in the $\alpha\beta$-frame. The positive-frequency and negative-frequency of complex space vectors in the $\alpha\beta$-frame imply that the positive-sequence and negative-sequence components of three-phase systems. For a given vector at the frequency ω, a frequency-coupled vector at the frequency $2\omega_1 - \omega$ is yielded from (34). Hence, only when the frequency ω is above $2\omega_1$, there is a coupling between the positive-sequence and negative-sequence components. Otherwise, only the positive-sequence components at two different frequencies will be brought by the asymmetric transfer matrix.

Next is to apply this equivalence to the VSC control output admittance including the PLL dynamics, i.e., to transform the admittance matrix given in (24) from the *dq*-frame to the

$\alpha\beta$-frame. In (19), the q-axis voltage V_q is replaced by the complex space vectors as follows:

$$V_q = \frac{\mathbf{V_{dq}} - \mathbf{V}^*_{\mathbf{dq}}}{2j} \tag{35}$$

which consequently leads to

$$\mathbf{I}_{\mathbf{PLL},\mathbf{dq}} = \underbrace{\frac{H_{\mathrm{PLL}}(s)\mathbf{I}_{\mathbf{1},\mathbf{dq}}}{2}}_{\mathbf{Y_{PLL}}(s)} \left(\mathbf{V_{dq}} - \mathbf{V}^*_{\mathbf{dq}}\right) \tag{36}$$

$$\mathbf{V}_{\mathbf{PLL},\mathbf{dq}} = \underbrace{\frac{H_{\mathrm{PLL}}(s)\mathbf{V}_{\mathbf{c1},\mathbf{dq}}}{2}}_{\mathbf{G_{PLL}}(s)} \left(\mathbf{V_{dq}} - \mathbf{V}^*_{\mathbf{dq}}\right) \tag{37}$$

where $\mathbf{Y_{PLL}}(s)$ and $\mathbf{G_{PLL}}(s)$ are the equivalent complex transfer functions of asymmetric transfer matrices $Y^m_{PLL}(s)$ and $Y^m_{PLL}(s)$ given in (22), respectively.

The modified open-loop output admittance is formulated by using complex transfer functions and complex space vectors, which is given by

$$\mathbf{I_{dq}}|_{\mathbf{V}_{\mathbf{o},\mathbf{dq}}=0} = \underbrace{\left[\mathbf{Y}_{\mathbf{o},\mathbf{dq}}(s) - G_d(s)\mathbf{Y}_{\mathbf{p},\mathbf{dq}}(s)\mathbf{G_{PLL}}(s)\right]}_{\mathbf{Y}_{\mathbf{to+},\mathbf{dq}}(s)} \mathbf{V_{dq}} + \underbrace{G_d(s)\mathbf{Y}_{\mathbf{p},\mathbf{dq}}(s)\mathbf{G_{PLL}}(s)}_{\mathbf{Y}_{\mathbf{to-},\mathbf{dq}}(s)} \mathbf{V}^*_{\mathbf{dq}} \tag{38}$$

where $\mathbf{Y}_{\mathbf{to+},\mathbf{dq}}(s)$ and $\mathbf{Y}_{\mathbf{to-},\mathbf{dq}}(s)$ are the complex transfer functions of the modified open-loop output admittance. Thus, the transfer matrix given in (23) is equivalent to two complex transfer functions. Then taking (36) into account, the modified closed-loop control output admittance can be derived by

$$\mathbf{I_{dq}}|_{\mathbf{I}_{\mathbf{ref},\mathbf{dq}}=0} = \underbrace{\left[-\mathbf{G}_{\mathbf{cl},\mathbf{dq}}(s)\mathbf{Y_{PLL}}(s) + \frac{\mathbf{Y}_{\mathbf{to+},\mathbf{dq}}(s)}{1+\mathbf{T_{dq}}(s)}\right]}_{\mathbf{Y}_{\mathbf{tcl+},\mathbf{dq}}(s)} \mathbf{V_{dq}} + \underbrace{\left[\mathbf{G}_{\mathbf{cl},\mathbf{dq}}(s)\mathbf{Y_{PLL}}(s) + \frac{\mathbf{Y}_{\mathbf{to-},\mathbf{dq}}(s)}{1+\mathbf{T_{dq}}(s)}\right]}_{\mathbf{Y}_{\mathbf{tcl-},\mathbf{dq}}(s)} \mathbf{V}^*_{\mathbf{dq}} \tag{39}$$

where $\mathbf{Y}_{\mathbf{tcl+},\mathbf{dq}}(s)$ and $\mathbf{Y}_{\mathbf{tcl-},\mathbf{dq}}(s)$ are complex transfer functions of the modified closed-loop control output admittance.

Following the same procedure as (30), the complex transfer matrix of the modified closed-loop control output admittance can be given, in the dq-frame, as

$$\begin{bmatrix}\mathbf{I_{dq}}\\ \mathbf{I}^*_{\mathbf{dq}}\end{bmatrix} = \underbrace{\begin{bmatrix}\mathbf{Y}_{\mathbf{tcl+},\mathbf{dq}}(s) & \mathbf{Y}_{\mathbf{tcl-},\mathbf{dq}}(s)\\ \mathbf{Y}^*_{\mathbf{tcl-},\mathbf{dq}}(s) & \mathbf{Y}^*_{\mathbf{tcl+},\mathbf{dq}}(s)\end{bmatrix}}_{\mathbf{Y}^{\mathbf{m}}_{\mathbf{tcl\pm},\mathbf{dq}}(s)} \begin{bmatrix}\mathbf{V_{dq}}\\ \mathbf{V}^*_{\mathbf{dq}}\end{bmatrix}. \tag{40}$$

Finally, applying the frequency translation formulated in (32) and (33), the dq-frame complex transfer matrix is transformed into the $\alpha\beta$-frame, which is expressed by

$$\begin{bmatrix}\mathbf{I}\\ e^{j2\theta}\mathbf{I}^*\end{bmatrix} = \underbrace{\begin{bmatrix}\mathbf{Y}_{\mathbf{tcl+},\mathbf{dq}}(s-j\omega_1) & \mathbf{Y}_{\mathbf{tcl-},\mathbf{dq}}(s-j\omega_1)\\ \mathbf{Y}^*_{\mathbf{tcl-},\mathbf{dq}}(s-j\omega_1) & \mathbf{Y}^*_{\mathbf{tcl+},\mathbf{dq}}(s-j\omega_1)\end{bmatrix}}_{\mathbf{Y}^{\mathbf{m}}_{\mathbf{tcl\pm}}(s)} \times \begin{bmatrix}\mathbf{V}\\ e^{j2\theta}\mathbf{V}^*\end{bmatrix} \tag{41}$$

where $\mathbf{Y}^{\mathbf{m}}_{\mathbf{tcl\pm}}(s)$ is the $\alpha\beta$-frame VSC control output admittance matrix including the PLL dynamics.

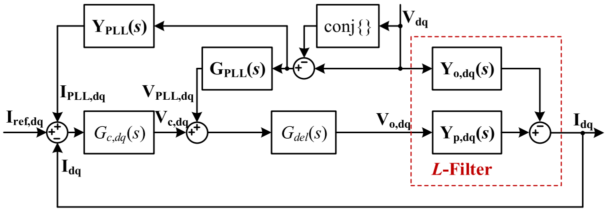

Fig. 6. Block diagram of complex transfer functions of the dq-frame current control with the PLL effect.

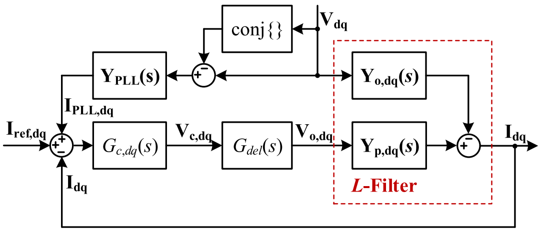

Fig. 7. Block diagram of complex transfer functions of the $\alpha\beta$-frame current control with the PLL effect.

B. Impedance Shaping Effect of PLL

Fig. 6 shows the equivalent block diagram of Fig. 5, where, according to (36) and (37), complex space vectors and complex transfer functions are used to replace the real space vectors and transfer matrices in Fig. 5. It is shown that the PLL dynamics introduce the frequency-coupling dynamics with the complex conjugate of the PCC voltage. Also, the PLL dynamics modify the inputs of both the current controller and the modulator in the dq-frame current control, which consequently shapes both the open-loop output admittance, see (38), and the closed-loop control output admittance.

Fig. 7 illustrates the block diagram of the $\alpha\beta$-frame current control loop with the PLL dynamics, where the current control loop is transformed into the dq-frame, following the frequency translation given in (2) and (4). Similar to (17), the PLL effect on the current reference can be derived as

$$\begin{aligned}\mathbf{I_{ref}} &= \mathbf{I}_{\mathbf{ref},\mathbf{dq}}e^{j\theta} = (\mathbf{I}_{\mathbf{ref1},\mathbf{dq}} + \Delta\mathbf{I_{dq}})e^{j(\omega_1 t+\Delta\theta)}\\ &\approx (\mathbf{I}_{\mathbf{1},\mathbf{dq}} + \Delta\mathbf{I_{dq}})(1+j\Delta\theta)e^{j\omega_1 t}\\ &\Rightarrow \mathbf{I}_{\mathbf{ref},\mathbf{dq}} = \mathbf{I}_{\mathbf{ref1},\mathbf{dq}} + \Delta\mathbf{I_{dq}} + \Delta\mathbf{I}_{\mathbf{PLL},\mathbf{dq}}\\ \Delta\mathbf{I}_{\mathbf{PLL},\mathbf{dq}} &= j\Delta\theta\mathbf{I}_{\mathbf{ref1},\mathbf{dq}} = j\Delta\theta\mathbf{I}_{\mathbf{1},\mathbf{dq}}\end{aligned} \tag{42}$$

TABLE II
CURRENT CONTROLLER AND PLL PARAMETERS

Symbol	Controller Parameter	Value
k_p	Proportional gain of current controller	16 Ω
k_i	Integral gain of current controller	600 Ω/s
k_{p_PLL}	PLL-proportional gain ($f_{\mathrm{PLL}} = 20$ Hz)	1.08 rad/s
	PLL-proportional gain ($f_{\mathrm{PLL}} = 175$ Hz)	9.51 rad/s
	PLL-proportional gain ($f_{\mathrm{PLL}} = 330$ Hz)	18.07 rad/s
k_{i_PLL}	PLL-integral gain ($f_{\mathrm{PLL}} = 20$ Hz)	99.75 rad/s^2
	PLL-integral gain ($f_{\mathrm{PLL}} = 175$ Hz)	7675 rad/s^2
	PLL-integral gain ($f_{\mathrm{PLL}} = 330$ Hz)	27 708 rad/s^2

where $\mathbf{I_{ref1,dq}}$ is the current reference at the steady-state, which is equal to $\mathbf{I_{1,dq}}$. Thus, the same effect on the input of the current controller as the *dq*-frame current control is brought by the PLL. However, differing from Fig. 6, the PLL dynamics have no effect on the input of the modulator and the open-loop output admittance. This difference is because the center frequency of the R controller, i.e., the grid fundamental frequency ω_1, is fixed in the $\alpha\beta$-frame current control scheme shown in Fig. 2(a). In contrast, the I controller in the *dq*-frame leads to an equivalent R controller with the center frequency varied with the dynamics of the PLL [2], [8].

V. IMPEDANCE-BASED STABILITY ANALYSIS

The generalized Nyquist stability criterion is widely applied to the asymmetric impedance matrices for the system stability assessment [22], [23]. Similar to the *dq*-frame impedance model, the proposed $\alpha\beta$-frame impedance model is asymmetric, which requires using the generalized Nyquist stability criterion for the converter–grid interaction analysis. Considering the grid impedance, the impedance ratio is given by

$$\mathbf{L^m}(s) = \mathbf{Z_g^m}(s)\mathbf{Y^m_{tcl\pm}}(s) \tag{43}$$

where $Z_g^m(s)$ is the grid impedance matrix. The system stability can then be predicted based on the frequency responses of the eigenvalues of the impedance ratio, which are derived by

$$\det\left[\lambda I^m - \mathbf{Z_g^m}(s)\mathbf{Y^m_{tcl\pm}}(s)\right] = 0. \tag{44}$$

Since the grid impedance is assumed to be balanced, the grid impedance matrix turns as a diagonal matrix for the complex space vectors. Corresponding to the *dq*-frame complex transfer matrix of the VSC control output admittance, which is given by (40), the grid impedance matrix can be expressed as

$$\begin{aligned} Z_g(s) &= \frac{L_g s + R_{Lg}}{(L_g s + R_{Lg})C_g s + 1} \\ \Rightarrow \mathbf{Z_{g,dq}}(s) &= \frac{L_g(s + j\omega_1) + R_{Lg}}{[L_g(s + j\omega_1) + R_{Lg}]\, C_g(s + j\omega_1) + 1} \end{aligned} \tag{45}$$

$$\begin{bmatrix} \mathbf{V_{dq}} \\ \mathbf{V^*_{dq}} \end{bmatrix} = \begin{bmatrix} \mathbf{V_{g,dq}} \\ \mathbf{V^*_{g,dq}} \end{bmatrix} - \underbrace{\begin{bmatrix} \mathbf{Z_{g,dq}}(s) & 0 \\ 0 & \mathbf{Z^*_{g,dq}}(s) \end{bmatrix}}_{\mathbf{Z^m_{g,dq}}(s)} \begin{bmatrix} \mathbf{I_{dq}} \\ \mathbf{I^*_{dq}} \end{bmatrix} \tag{46}$$

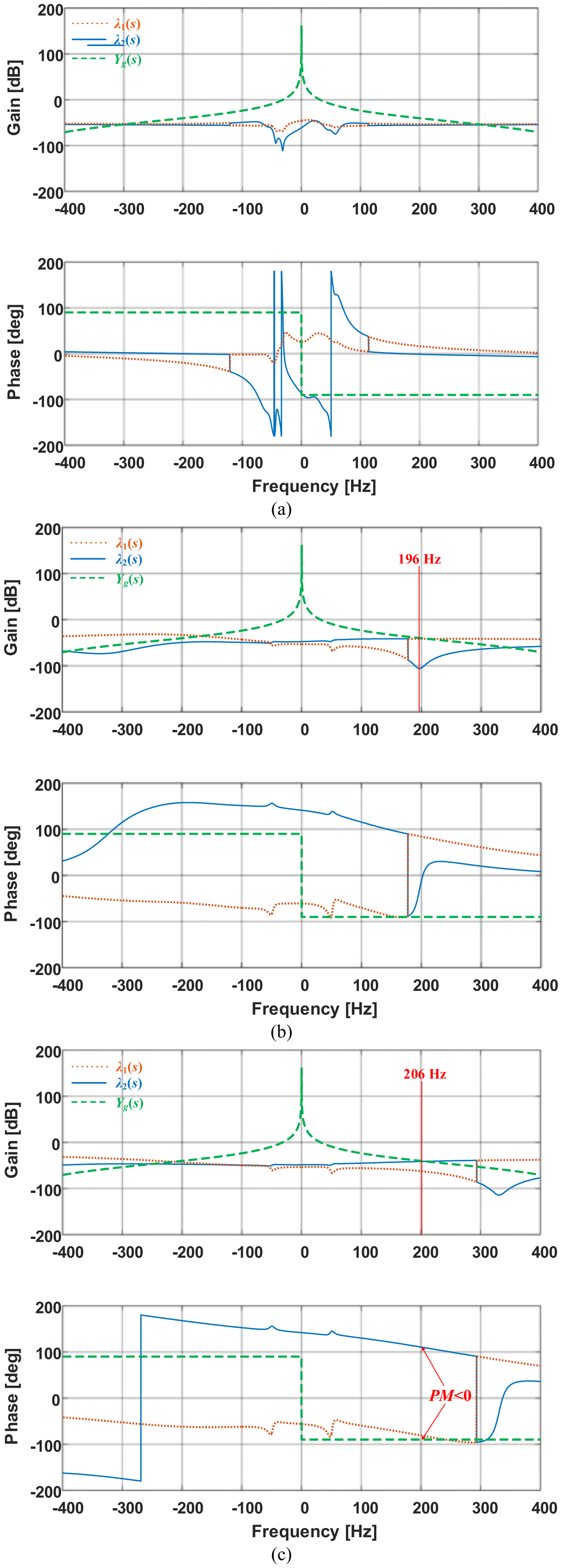

(a)

(b)

(c)

Fig. 8. Frequency responses for the eigenvalues of $\mathbf{Y(s)}$ and the grid impedance when using the *dq*-frame current control. (a) $f_{\mathrm{PLL}} = 20$ Hz. (b) $f_{\mathrm{PLL}} = 175$ Hz. (c) $f_{\mathrm{PLL}} = 330$ Hz.

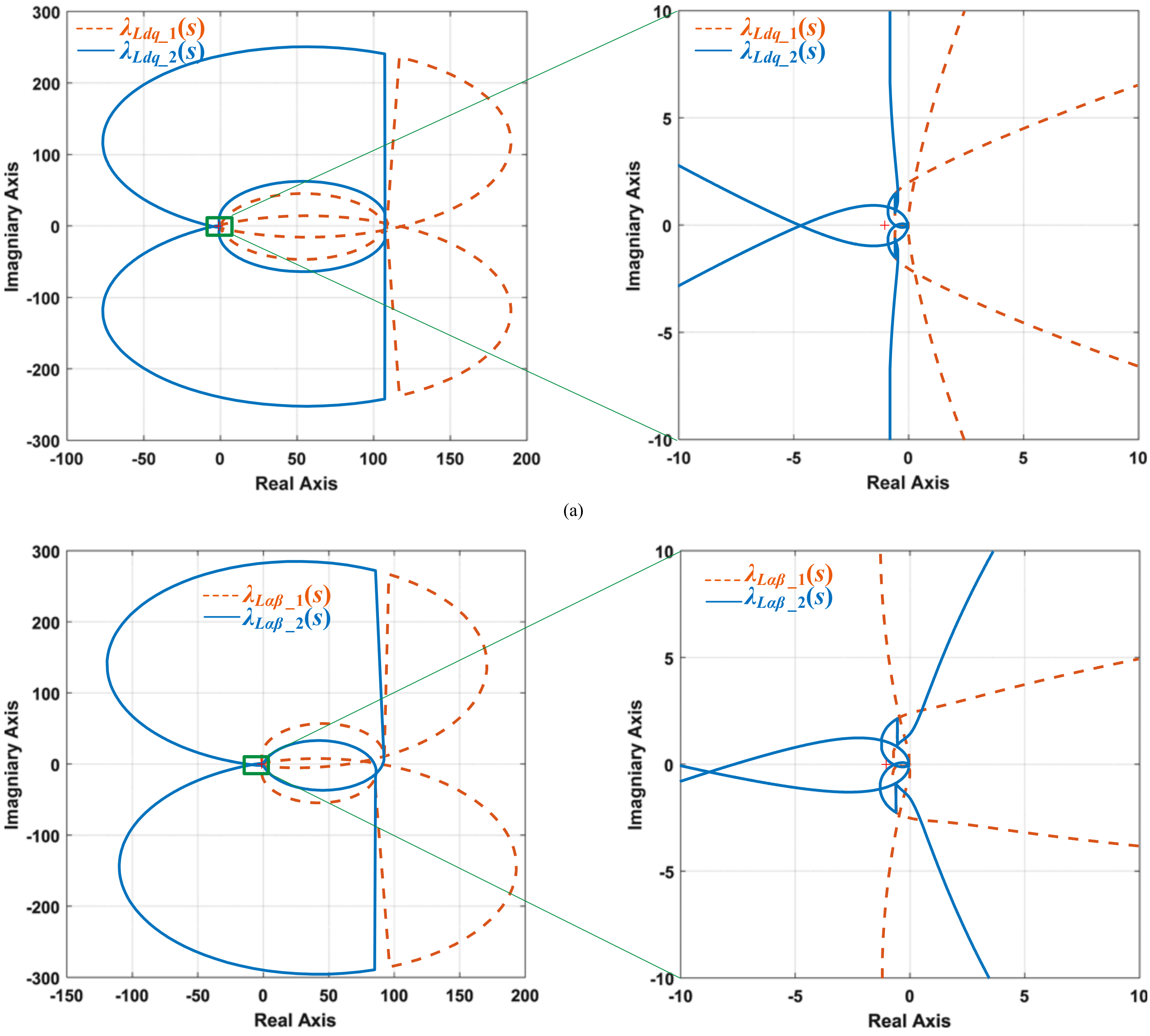

Fig. 9. Nqyuist diagrams for the eigenvalues of the impedance ratios derived in different domains. (a) *dq*-frame impedance model. (b) $\alpha\beta$-frame impedance model.

where R_{Lg} is the equivalent series resistance of grid inductance L_g. The complex conjugate of $\mathbf{Z}_{\mathrm{g,dq}}(s)$ is given by

$$\mathbf{Z}^*_{\mathrm{g,dq}}(s) = \frac{L_g(s-j\omega_1)+R_{Lg}}{[L_g(s-j\omega_1)+R_{Lg}]\,C_g(s-j\omega_1)+1} \qquad (47)$$

which can then be transformed into the $\alpha\beta$-frame following the frequency translation given in (32) and (33), and it is given by

$$\mathbf{Z}^{\mathrm{m}}_{\mathrm{g,dq}}(s) \to \mathbf{Z}^{\mathrm{m}}_{\mathrm{g}}(s) = \begin{bmatrix} \mathbf{Z}_{\mathrm{g,dq}}(s-j\omega_1) & 0 \\ 0 & \mathbf{Z}^*_{\mathrm{g,dq}}(s-j\omega_1) \end{bmatrix} = \begin{bmatrix} Z_g(s) & 0 \\ 0 & Z_g(s-j2\omega_1) \end{bmatrix}. \qquad (48)$$

With the diagonal grid impedance matrix, the eigenvalues of the impedance ratio can be approximated as

$$\det\left[\lambda I^m - \mathbf{Z}^{\mathrm{m}}_{\mathrm{g}}(s)\mathbf{Y}^{\mathrm{m}}_{\mathrm{tcl}\pm}(s)\right] \approx Z_g(s)\cdot\det\left[\lambda I^m - \mathbf{Y}^{\mathrm{m}}_{\mathrm{tcl}\pm}(s)\right]. \qquad (49)$$

Instead of plotting the Nyquist diagrams for the eigenvalues of (44), the converter–grid interactions can be analyzed by plotting the frequency responses for the eigenvalues of $\mathbf{Y}^{\mathrm{m}}_{\mathrm{tcl}\pm}(s)$ against the grid admittance, i.e., $Y_g(s) = 1/Z_g(s)$. The system stability will be dependent on the phase difference at the frequencies where their magnitude responses intersect, where the phase difference out of 180° indicates an unstable system with a negative phase margin [18].

Table II provides the controller parameters used in this work. Three sets of SRF-PLL parameters with the different control bandwidth f_{PLL} are evaluated. The control bandwidth of the SRF-PLL is determined by the settling time, T_{set}, of the second-order system given by (19), i.e., $f_{\mathrm{PLL}} \approx 1/T_{\mathrm{set}}$, where the damping ratio is chosen as 0.707, and the parameters of the PI controller can be found based on the settling time [14].

First, considering the cases with the *dq*-frame current control, the frequency responses for the eigenvalues of $\mathbf{Y}^{\mathbf{m}}_{\mathbf{tcl}\pm}(s)$ are plotted against the grid admittance. With the PLL bandwidth of 20 Hz, $f_{\mathrm{PLL}} = 20$ Hz, the phase differences at the frequencies where $|\lambda_1(j\omega)| = |Y_g(j\omega)|$ or $|\lambda_2(j\omega)| = |Y_g(j\omega)|$ are within 180°, as shown in Fig. 8(a), which imply a stable response of the VSC system. However, as the PLL bandwidth increases, the phase differences are increased.

Fig. 8(b) plots the frequency responses for $f_{\mathrm{PLL}} = 175$ Hz, where the phase difference at their magnitude intersection frequency 196 Hz is close to 180°. This implies that the system is marginally stable in response with the resonant or unexpected harmonic component nearby 196 Hz, and another frequency-coupled component nearby $2\omega_1 - \omega$, i.e., –96 Hz (negative-sequence), due to the frequency-coupling dynamics. When the PLL bandwidth is increased up to 330 Hz, the system becomes unstable with the phase difference out of 180° at the magnitude-interaction frequency, as shown in Fig. 8(c).

Fig. 9 then compares the Nyquist diagrams of the eigenvalues of the impedance ratio derived from the *dq*-frame impedance model and the $\alpha\beta$-frame impedance model, where the case of the *dq*-frame current control with the PLL bandwidth of 330 Hz is considered. The same instability implication can be observed from the two Nyquist diagrams. Yet, differing from the *dq*-frame impedance model, the Nyquist diagrams of the $\alpha\beta$-frame impedance model are asymmetric between the positive- and negative-frequencies. This difference is brought by the frequency translation from the *dq*-frame to the $\alpha\beta$-frame. It is worth noting that the *dq*-frame complex transfer matrix, which is given in (40), leads to the same Nyquist diagrams as the *dq*-frame impedance matrix of real space vectors. This equivalence has been explicitly elaborated in [17].

Subsequently, Fig. 10 depicts the frequency responses for the cases with the $\alpha\beta$-frame current control. Differing from the *dq*-frame current control, the VSC is kept stable with all three sets of PLL parameters. The differences are due to the use of a fixed-frequency R controller in the $\alpha\beta$-frame, which, as illustrated in Fig. 7, equivalently avoids the PLL effect on the modulating voltage, and it is hence more robust against the dynamic impact of the PLL than the *dq*-frame current control.

However, similar to the *dq*-frame current control, the system phase margin is also reduced, i.e., the phase difference at the intersection frequencies of the magnitude responses is getting closer to 180°, as the bandwidth of the PLL increases. Fig. 10(c) shows that a marginally stable operation with the under-damped resonance may be resulted at the intersection frequency (270 Hz) of the magnitude responses, and the frequency-coupling harmonic at 170 H, yet in the negative-sequence, may arise.

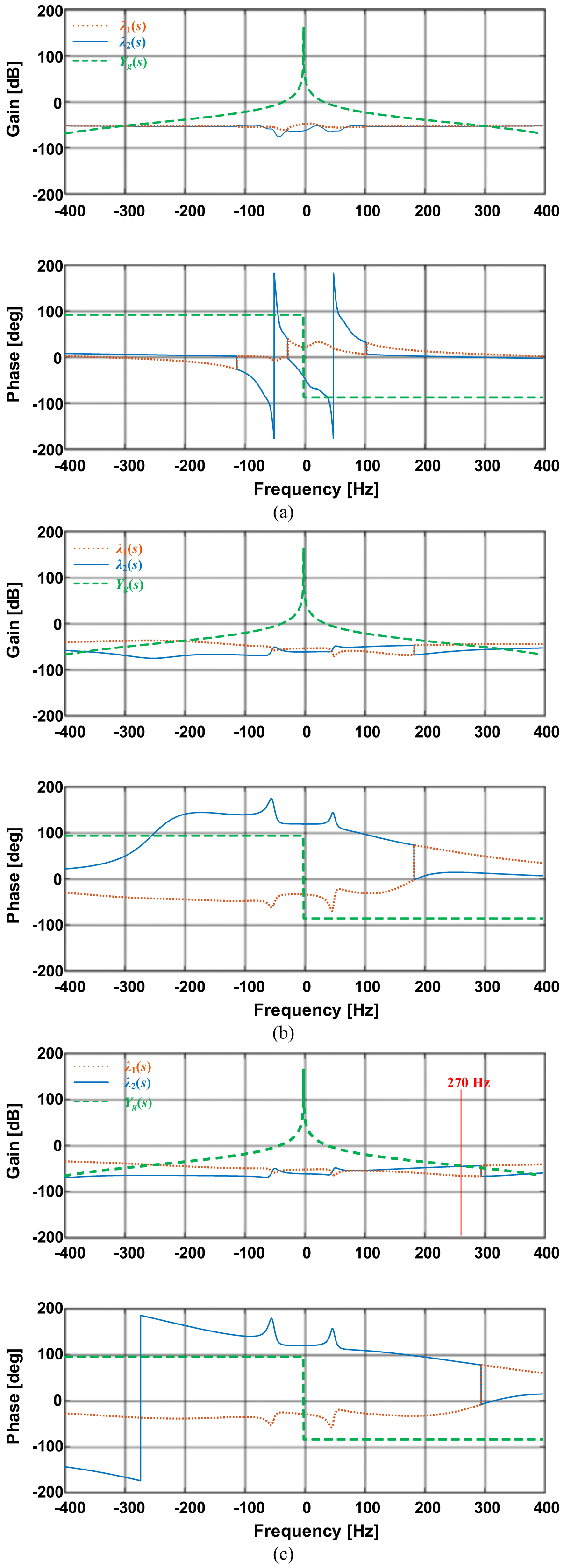

Fig. 10. Frequency responses for the eigenvalues of **Y(s)** and the grid impedance when using the $\alpha\beta$-frame current control. (a) $f_{\mathrm{PLL}} = 20$ Hz. (b) $f_{\mathrm{PLL}} = 175$ Hz. (c) $f_{\mathrm{PLL}} = 330$ Hz.

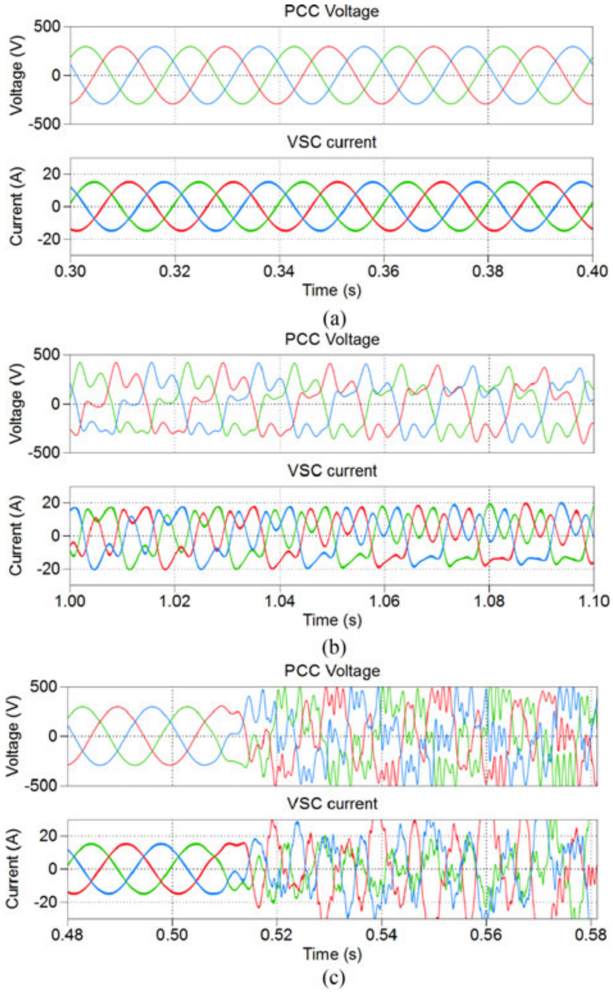

Fig. 11. Simulated PCC voltage and VSC current for the *dq*-frame current control. (a) $f_{\mathrm{PLL}} = 20$ Hz. (b) $f_{\mathrm{PLL}} = 175$ Hz. (c) $f_{\mathrm{PLL}} = 330$ Hz.

VI. Simulations and Experimental Results

A. Simulation Results

To verify the effectiveness of the impedance-based analysis, the time-domain simulations based on the MATLAB/Simulink and PLECS blockset are performed. The parameters presented in Tables I and II are adopted.

Fig. 11 shows the simulated PCC voltage (line-to-line) and VSC current for the *dq*-frame current control. Three cases corresponding to the three different sets of PLL parameters are compared. A stable response is observed in Fig. 11(a) when $f_{\mathrm{PLL}} = 20$ Hz, which agrees with the frequency-domain analysis in Fig. 8(a). Fig. 11(b) depicts the simulated waveforms for the case of $f_{\mathrm{PLL}} = 175$ Hz, where the harmonic distortions confirm the stability implication of Fig. 8(b). Fig. 12 further illustrates the harmonic spectra analysis of Fig. 11(b), where the two main harmonic components correlate closely with the frequency identified in Fig. 8(b), and phase sequence obtained in the harmonic spectra verifies the frequency coupling effect, i.e., $2\omega_1 - \omega$. Fig. 11(c) shows the step change of the PLL bandwidth from 20 to 330 Hz at the time instant of 0.5 s. It is clear that the system becomes unstable when the PLL bandwidth is increased.

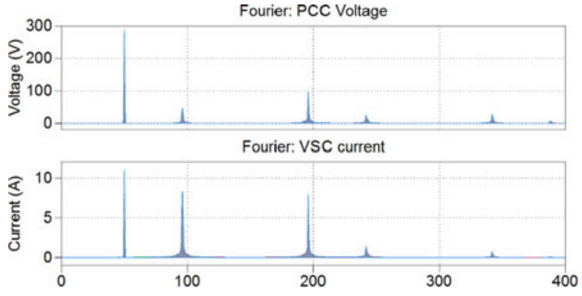

Fig. 12. Harmonic spectra analysis for the simulated waveforms in Fig. 11(b).

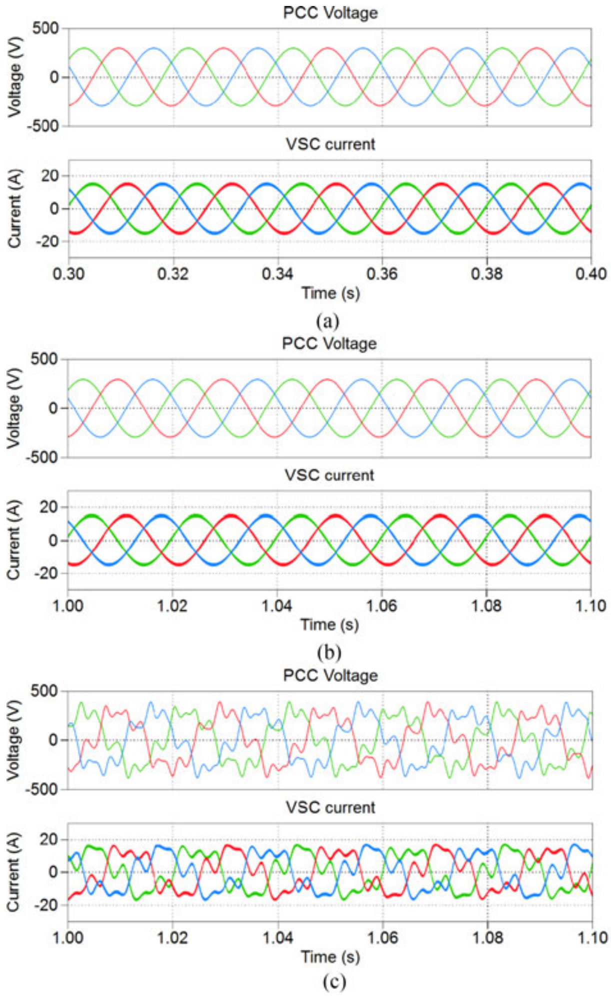

Fig. 13. Simulated PCC voltage and VSC current for the $\alpha\beta$-frame current control. (a) $f_{\mathrm{PLL}} = 20$ Hz. (b) $f_{\mathrm{PLL}} = 175$ Hz. (c) $f_{\mathrm{PLL}} = 330$ Hz.

Fig. 13 shows the simulated results for the $\alpha\beta$-frame current control. It is clear that the system is kept stable in all cases, which confirms the stability analysis in Fig. 10. The harmonic distortion shown in Fig. 13(c) verifies the limited phase margin predicted in Fig. 10(c). The harmonic spectra of Fig. 13(c) are shown in Fig. 14, where the two harmonic components confirm the frequency identified in Fig. 10(c) and the coupled harmonic distortion.

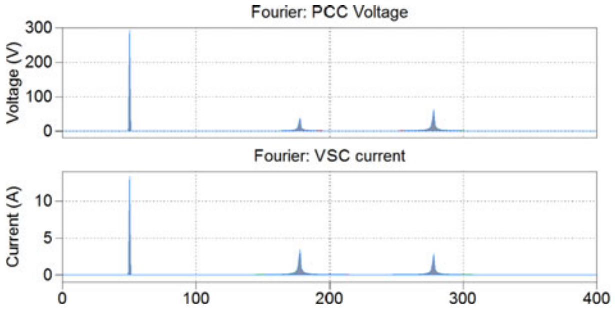

Fig. 14. Harmonic spectra analysis for the simulated waveforms in Fig. 13(c).

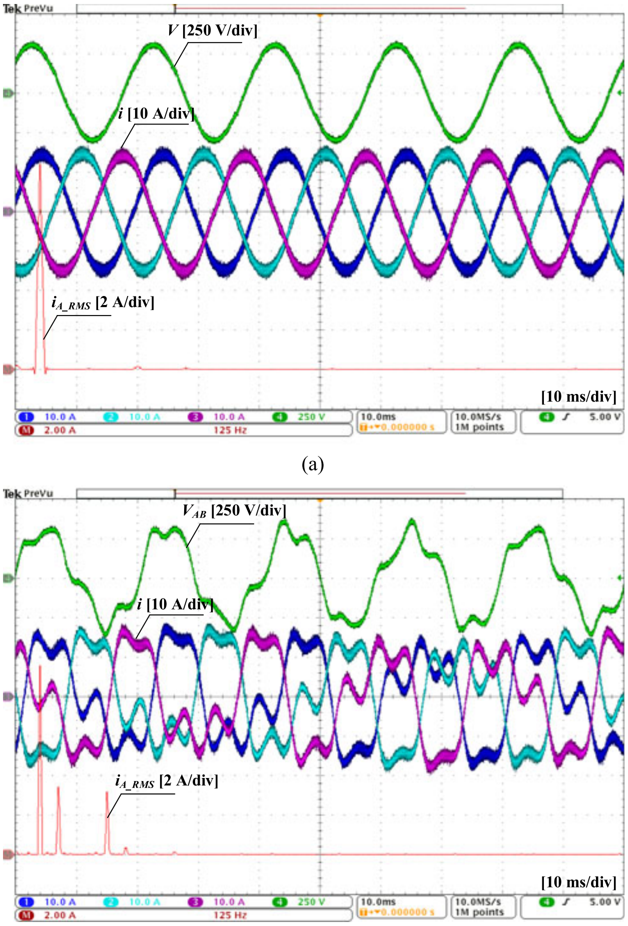

(a)

(b)

Fig. 15. Measured PCC voltage and VSC current for the *dq*-frame current control. (a) $f_{\rm PLL} = 20$ Hz. (b) $f_{\rm PLL} = 175$ Hz.

B. Experimental Results

To further verify the simulation results, the experiments on a laboratory test setup are carried out. All the parameters used in the frequency-domain analysis and time-domain simulations are tested in experiments. A frequency converter is used as the grid-connected VSC. The control system is implemented in the DS1007 dSPACE system, where the DS5101 digital waveform output board is used for generating the switching pulses, and the DS2004 high-speed A/D board is used for the voltage and current measurements. A constant dc voltage supply is used at the dc-side, and Chroma grid simulator is used to generate the grid voltage.

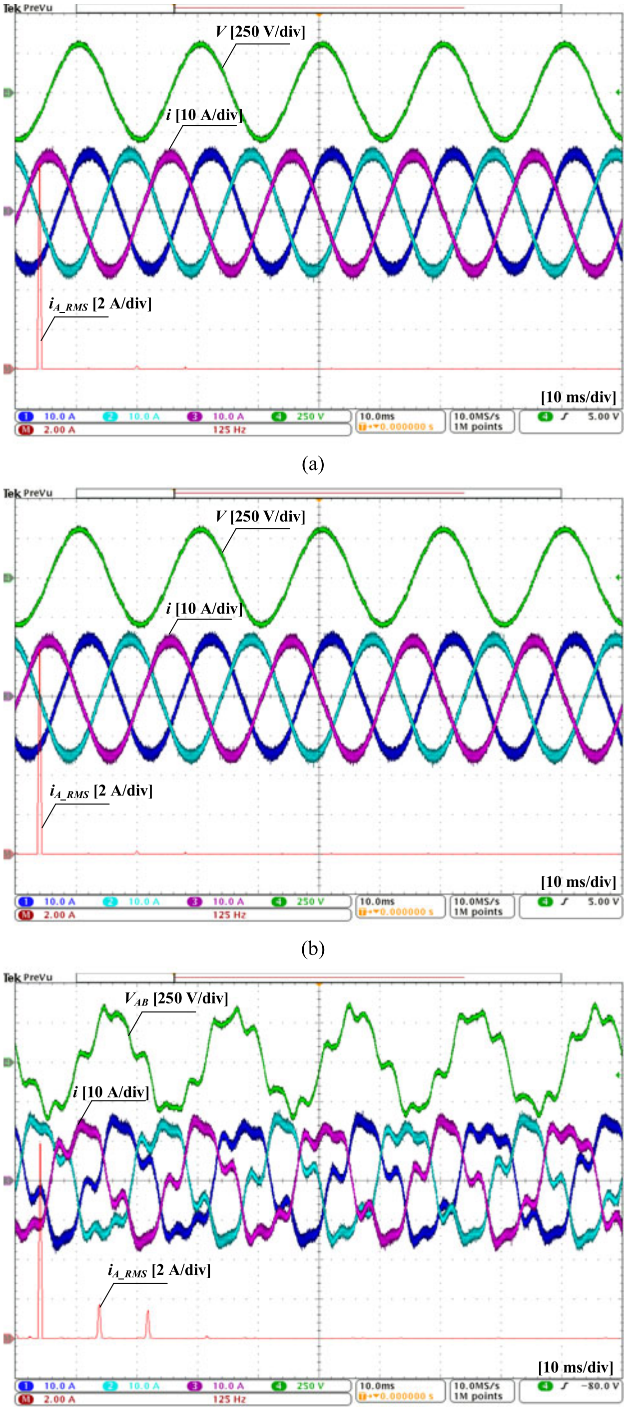

(a)

(b)

(c)

Fig. 16. Measured PCC voltage and VSC current for the $\alpha\beta$-frame current control. (a) $f_{\rm PLL} = 20$ Hz. (b) $f_{\rm PLL} = 175$ Hz. (c) $f_{\rm PLL} = 330$ Hz.

Fig. 15 shows the measured line-to-line PCC voltage $(V_{\rm AB})$ and VSC currents for the *dq*-frame current control. Two sets of PLL parameters, i.e., $f_{\rm PLL} = 20$ Hz and 175 Hz, are tested, since the unstable case with $f_{\rm PLL} = 330$ Hz tripped the test system. The harmonic spectra of the phase-A current are shown.

It is clear that the voltage and current are distorted when the PLL bandwidth is increased to $f_{\mathrm{PLL}} = 175$ Hz, which closely correlate with the simulation results in Fig. 11(a) and (b).

Fig. 16 shows the measured line-to-line PCC voltage (V_{AB}) and VSC currents for the $\alpha\beta$-frame current control. Three sets of PLL parameters presented in Table II are tested for comparison. It is clear that the harmonic spectra of the phase-A current in Fig. 16(c) match with the simulation result in Fig. 14 and the frequency identified in Fig. 10(c).

VII. CONCLUSION

This paper has discussed a unifying approach to the impedance models of VSCs with the PLL dynamics included. The mathematical relations between the models built in the different domains have been explicitly revealed. A complex equivalence of the asymmetric *dq*-frame impedance matrix has been introduced based on complex space vectors and complex transfer functions. Based on the complex equivalence, a stationary-frame ($\alpha\beta$-frame) impedance model has further been developed. Frequency-domain analysis on the influence of different PLL bandwidths has been performed with the developed impedance model, and validated in time domain simulations and experiments.

REFERENCES

[1] F. Blaabjerg, R. Teodorescu, M. Liserre, and A. Timbus, "Overview of control and grid synchronization for distributed power generation systems," *IEEE Trans. Ind. Electron.*, vol. 53, no. 5, pp. 1398–1409, Oct. 2006.

[2] L. Harnefors, X. Wang, A. G. Yepes, and F. Blaabjerg, "Passivity-based stability assessment of grid-connected VSCs—An overview," *IEEE J. Emerging Sel. Topics Power Electron.*, vol. 4, no. 1, pp. 116–125, Mar. 2016.

[3] X. Wang, F. Blaabjerg, and W. Wu, "Modeling and analysis of harmonic stability in ac power-electronics-based power system," *IEEE Trans. Power Electron.*, vol. 29, no. 12, pp. 6421–6432, Dec. 2014.

[4] X. Wang, F. Blaabjerg, M. Liserre, Z. Chen, Y. W. Li, and J. He, "An active damper for stabilizing power-electronics-based ac systems," *IEEE Trans. Power Electron.*, vol. 29, no. 7, pp. 3318–3329, Jul. 2014.

[5] X. Wang, F. Blaabjerg, and P. C. Loh, "Proportional derivative based stabilizing control of paralleled grid converters with cables in renewable power plants," in *Proc. 2014 IEEE Energy Convers. Congr. Expo.*, 2014, pp. 4917–4924.

[6] L. Harnefors, A. G. Yepes, A. Vidal, and J. Doval-Gandoy, "Passivity-based controller design of grid-connected VSCs for prevention of electrical resonance instability," *IEEE Trans. Ind. Electron.*, vol. 62, no. 2, pp. 702–710, Feb. 2015.

[7] L. Harnefors, M. Bongiorno, and S. Lundberg, "Input-admittance calculation and shaping for controlled voltage-source converters," *IEEE Trans. Ind. Electron.*, vol. 54, no. 6, pp. 3323–3334, Dec. 2007.

[8] B. Wen, D. Boroyevich, R. Burgos, P. Mattavelli, and Z. Shen, "Analysis of D-Q small-signal impedance of grid-tied inverters," *IEEE Trans. Power Electron.*, vol. 31, no. 1, pp. 675–687, Jan. 2016.

[9] B. Wen, D. Dong, D. Boroyevich, R. Burgos, P. Mattavelli, and Z. Shen, "Impedance-based analysis of grid-synchronization stability for three-phase paralleled converters," *IEEE Trans. Power Electron.*, vol. 31, no. 1, pp. 26–38, Jan. 2016.

[10] M. Cespedes and J. Sun, "Impedance modeling and analysis of grid-connected voltage-source converters," *IEEE Trans. Power Electron.*, vol. 29, no. 3, pp. 1254–1261, Mar. 2014.

[11] S. K. Chung, "A phase tracking system for three phase utility interface inverters," *IEEE Trans. Power Electron.*, vol. 15, no. 3, pp. 431–438, May 2000.

[12] P. Rodriguez, J. Pou, J. Bergas, J. Candela, R. Burgos, and D. Boroyevich, "Decoupled double synchronous reference frame PLL for power converters control," *IEEE Trans. Power Electron.*, vol. 22, no. 2, pp. 584–592, Mar. 2007.

[13] M. Karimi-Ghartemani, "A unifying approach to single-phase synchronous reference frame PLLs," *IEEE Trans. Power Electron.*, vol. 28, no. 10, pp. 4550–4556, Oct. 2013.

[14] R. Teodorescu, M. Liserre, and P. Rodriguez, *Grid Converters for Photovoltaic and Wind Power Systems*. Hoboken, NJ, USA: Wiley, 2011.

[15] L. Harnefors, "Modeling of three-phase dynamic systems using complex transfer functions and transfer matrices," *IEEE Trans. Ind. Electron.*, vol. 54, no. 4, pp. 2239–2248, Aug. 2007.

[16] M. K. Bakhshizadeh, X. Wang, F. Blaabjerg, J. Hjerrild, L. Kocewiak, C. L. Bak, and B. Hesselbaek, "Couplings in phase domain impedance modeling of grid-connected converters," *IEEE Trans. Power Electron.*, vol. 31, no. 10, pp. 6792–6796, Oct. 2016.

[17] A. Rygg, M. Molinas, C. Zhang, and X. Cai, "A modified sequence domain impedance definition and its equivalence to the dq-domain impedance definition for the stability analysis of ac power electronic systems," *IEEE J. Emerging Sel. Topics Power Electron.*, vol. 4, no. 4, pp. 1383–1396, Dec. 2016.

[18] R. Turner, S. Walton, and R. Duke, "A case study on the application of the Nyquist stability criterion as applied to the interconnected loads and sources on grids," *IEEE Trans. Ind. Electron.*, vol. 60, no. 7, pp. 2740–2749, Jul. 2013.

[19] J. Sun, "Small-signal methods for ac distributed power systems—A review," *IEEE Trans. Power Electron.*, vol. 24, no. 11, pp. 2545–2554, Nov. 2009.

[20] S. Buso and P. Mattavelli, *Digital Control in Power Electronics*. San Rafael, CA, USA: Morgen & Claypool Publishers, 2006.

[21] X. Wang, Y. W. Li, F. Blaabjerg, and P. C. Loh, "Virtual-impedance-based control for voltage- and current-source converters," *IEEE Trans. Power Electron.*, vol. 30, no. 12, pp. 7019–7037, Dec. 2015.

[22] M. Belkhayat, "Stability criteria for ac power systems with regulated loads," Ph.D. dissertation, Purdue Univ., West Lafayette, IN, USA, Dec. 1997.

[23] B. Wen, D. Boroyevich, R. Burgos, P. Mattavelli, and Z. Shen, "Small-signal stability analysis of three-phase ac systems in the presence of constant power loads based on measured d-q frame impedances," *IEEE Trans. Power Electron.*, vol. 30, no. 10, pp. 5952–5963, Dec. 2015.

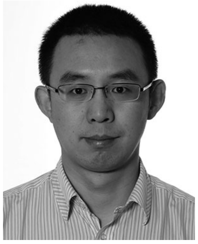

Xiongfei Wang (S'10–M'13) received the B.S. degree from Yanshan University, Qinhuangdao, China, in 2006, the M.S. degree from Harbin Institute of Technology, Harbin, China, in 2008, both in electrical engineering, and the Ph.D. degree in energy technology from Aalborg University, Aalborg, Denmark, in 2013. Since 2009, he has been with the Aalborg University, Aalborg, Denmark, where he is currently an Associate Professor in the Department of Energy Technology. His research interests include modeling and control of grid-connected converters, harmonics analysis and control, passive and active filters, stability of power electronic based power systems.

Dr. Wang serves as an Associate Editor for the IEEE TRANSACTIONS ON POWER ELECTRONICS, the IEEE TRANSACTIONS ON INDUSTRY APPLICATIONS, and the IEEE JOURNAL OF EMERGING AND SELECTED TOPICS IN POWER ELECTRONICS. He received the second prize paper award and the outstanding reviewer award of IEEE TRANSACTIONS ON POWER ELECTRONICS in 2014 and 2016, respectively, and the best paper awards at IEEE PEDG 2016 and IEEE PES General Meeting 2017.

Lennart Harnefors (S'93–M'97–SM'07–F'17) received the M.Sc., Licentiate, and Ph.D. degrees in electrical engineering from the Royal Institute of Technology (KTH), Stockholm, Sweden, and the Docent (D.Sc.) degree in industrial automation from Lund University, Lund, Sweden, in 1993, 1995, 1997, and 2000, respectively.

Between 1994 and 2005, he was with Mälardalen University, Västerås, Sweden, from 2001 as a Professor of electrical engineering. Between 2001 and 2005, he was, in addition, a part-time Visiting Professor of electrical drives with the Chalmers University of Technology, Goteborg, Sweden. Since 2005, he has been with ABB, where he is currently a Senior Principal Scientist in Corporate Research, Västerås, Sweden. He is, in addition, a part-time Adjunct Professor of power electronics with KTH. His research interests include control and dynamic analysis of power electronic systems, particularly grid-connected converters, ac drives, and wide-bandgap-transistor switching circuits.

Dr. Harnefors is an Associate Editor for the IEEE TRANSACTIONS ON INDUSTRIAL ELECTRONICS and the IET ELECTRIC POWER APPLICATIONS.

Frede Blaabjerg (S'86–M'88–SM'97–F'03) was working toward the Ph.D. degree in electrical engineering at Aalborg University, Aalborg, Denmark, from 1988 to 1992.

He was with ABB-Scandia, Randers, Denmark, from 1987 to 1988. He became an Assistant Professor in 1992, an Associate Professor in 1996, and a Full Professor of power electronics and drives in 1998. His current research interests include power electronics and its applications such as in wind turbines, PV systems, reliability, harmonics, and adjustable speed drives.

Dr. Blaabjerg received 17 IEEE Prize Paper Awards, the IEEE PELS Distinguished Service Award in 2009, the EPE-PEMC Council Award in 2010, the IEEE William E. Newell Power Electronics Award 2014, and the Villum Kann Rasmussen Research Award 2014. He was an Editor-in-Chief for the IEEE TRANSACTIONS ON POWER ELECTRONICS from 2006 to 2012. He is nominated in 2014 and 2015 by Thomson Reuters to be between the most 250 cited researchers in Engineering in the world.